Enhancing the Detection of Coastal Marine Debris in Very High-Resolution Satellite Imagery via Unsupervised Domain Adaptation

Kenichi Sasaki ⓘ , *Student Member, IEEE*, Tatsuyuki Sekine ⓘ , *Member, IEEE*, and William Emery ⓘ , *Fellow, IEEE*

Abstract—In this study, we propose a robust debris estimation model applied to satellite imagery that is suitable for practical applications. In our previous study, we proposed a coastal marine debris estimation model using semantic segmentation applied to very high-resolution satellite images. We identified limitations when applying the model to various lower spatial and spectral resolution satellite images or to areas with fewer satellite images cases. To overcome these limitations, we now employed unsupervised domain adaptation (UDA) techniques to transfer the earlier model to these lower resolution or fewer satellite images. These domain adaptation techniques consider differences in spatial feature distributions and/or satellite sensor characteristics. We confirmed the ability of UDA to classify Planet Skysat and Airbus Pleiades images using MAXAR WorldView images to generate an accurate segmentation map. The UDA, then, allows us to analyze the lower satellite images without the need to independently generate new segmentation labels. We conducted statistical analyses and demonstrated the high correlation between the local debris cleanup data and entropy metrics computed using our UDA approach. Our method enhances the sampling frequency of satellite images by analyzing lower resolution imagery, allowing monthly to weekly, or even daily intervals, and facilitates rapid estimation utilizing fewer images, thereby providing an invaluable tool for coastal debris characterization and assessment.

Index Terms—Marine debris, remote sensing, satellite imagery analysis, semantic segmentation, unsupervised domain adaptation (UDA), very high-resolution satellite images.

I. INTRODUCTION

MARINE debris poses a significant and widespread threat to the marine environment. It is transported by ocean currents and accumulates in coastal waters and on beaches from local to mesoscales (10–1000 km) [1], [2], [3]. The degradation of anthropogenic debris in the ocean results in the formation of increasingly smaller particles, making their detection and cleanup very challenging [4].

Policy-based organizations, such as the United Nations Environment Programme, have drawn public attention to the scope, magnitude, and impacts of marine pollution in recent decades [5]. Current developmental goals, such as those of the United Nations (UN) Agenda 2030 for Sustainable Development, approved in 2015, provide a long-term plan to encourage global action, including 17 Sustainable Development Goals (2015–2030) [6].

The current approach to marine debris on beaches is human physical cleanup, in areas of active fisheries or coastal recreation [7], [8]. The objective of these activities is to mitigate their impact on human activities. While these efforts are necessary and provide temporary relief in limited regions, it is important to recognize that the long-term impacts of anthropogenic debris extend beyond their influence on human activities. These long-term impacts apply to all marine animals and their habitats. The persistent presence of anthropogenic debris poses a threat to marine ecosystems [7], [9]. These changes in the marine environment eventually impact human activities, such as aquaculture. Over three billion people are known to depend on marine and coastal biodiversity for their livelihood [10].

Therefore, a long-term and comprehensive approach to identify and mitigate the impacts of marine debris is essential for effectively reducing their environmental impact. Research on identifying marine debris plays an important role in mitigating the impacts of marine debris, including environmental policy integration and the allocation of human resources. Our study focuses on using satellite imagery for the rapid assessment of debris deposition on beaches. By providing detailed information on marine debris deposition, we aim to support public agencies and local communities in making informed decisions to take appropriate actions to clean the beaches. Moreover, the dissemination of detailed information on debris deposition can contribute to raising social awareness about marine pollution. This increased awareness can drive long-term measures aimed at reducing the discharge of debris into the ocean including behavioral changes, such as the adoption of sustainable practices, the reduction of single-use plastics, and the implementation of proper waste management strategies [7], [11], [12].

A. Earlier Marine Debris Studies

We propose to use satellite imagery and aerial photography to estimate the deposition of coastal debris. We follow other

earlier studies that employ machine learning algorithms to detect anthropogenic debris, such as plastics [13], [14], [15], [16]. Most of these studies, however, achieved high accuracy only in limited areas or using only a few satellite images. These early machine learning models were trained by supervised learning, which trains the model using given ground truth data. So if you apply the model to other data or environments, the model performance is expected to be lower. Some studies also require a visual inspection of the imagery before the machine learning method can be applied [17], [18], [19], [20]. This process improves the model accuracy, but the required human intervention retards the speed of model deployment. Several researchers have used hyperspectral laboratory systems to characterize the spectral response of specific debris elements and then use supervised learning to analyze the satellite images to detect these elements [21], [22].

One study deployed several plastic sheets made of different materials and analyzed the spectral responses in the open ocean [23], [24]. Topouzelis et al. demonstrated the identification capability of $10\,\text{m} \times 10\,\text{m}$ sheets using Sentinel-1 and 2 images. Kikaki et al. introduced a database of marine debris using Sentinel 2 images [25]. Open-source (free) imagery enables marine debris studies and most studies are conducted using open-source satellite images, such as Landsat or Sentinel [26], [27]. Unfortunately, the spatial resolution of those images is significantly lower than the size of marine debris (10–30 m/pix). Consequently, the utilization of these satellites poses a challenge for achieving detailed debris characterization and early debris detection.

In addition, previous studies focus on detecting one single material, such as plastics [23], [28], [29] and then primarily under relatively restrictive conditions, such as the identification of manmade objects or in heavily contaminated regions. Most of the marine debris consists of and is entangled with a variety of components. On beaches, the debris has different backgrounds that are exposed to different weather conditions. Also, on the practical side, rapid deployment of the cleanup crew is crucial to prevent the re-entry of marine debris back into the open water. As a consequence, it is necessary to characterize coastal debris deposition to better manage its costly cleanup.

In our previous study, we proposed a new approach to identify the coastal debris density level based on the segmentation of WorldView 2 and 3 satellite imagery [30]. Our approach combined WorldView 2, 3, and coincident ground truth from coastal cleanup operations. This analysis was carried out for beaches on the islands of Okinawa in southern Japan where we have the regularly sampled clean-up data. We found a 0.72 correlation between the satellite image estimated debris and the ground truth clean-up data. Unlike other approaches, this model can differentiate between clean beaches and the early stages of debris deposition. However, this study was based on a semantic segmentation trained on only WorldView 2 and 3 images and the results do not apply to other satellite sensors with poorer resolutions, and to other areas with coverage of fewer satellite images, than were used in our study. Therefore, the ability to adapt the model to different satellite sensors or regions with limited image availability is needed to achieve higher temporal

sampling and enable rapid assessment on diverse beaches. The ultimate objective of the present study is to develop a robust estimation model capable of providing accurate estimates of beach debris solely from lower resolution or fewer satellite images.

B. Domain Adaptation

The ultimate ability of our debris estimation is directly dependent on the improvement of the segmentation model. The primary approach to designing robust semantic segmentation models is: 1) to train the model with a large dataset and 2) to employ unsupervised domain adaptation (UDA) to transfer the results from the model developed with the large dataset of satellite images with high spatial and spectral resolutions. In our previous study, many beaches in Japan were not covered with many high-resolution satellite images or were covered by satellite images of lower spatial and spectral resolutions. Therefore, we decided to use UDA to transfer the results from the data-rich region to other beaches on Japanese islands where fewer satellite images, or lower resolution images, and less ground truth data are available.

UDA carries knowledge from a label-rich source domain to an unlabeled weakly sampled target domain [31]. Thus, UDA can be viewed as a special case of transfer learning, where a model is trained on a source domain and then, applied to a similar target domain [32]. One method we can use to translate domain invariant features is using pixel-level adversarial training, such as a generative adversarial network (GAN) [33], [34]. Here, the generator performs the adaptation at the pixel level by translating a source input image to an image that closely resembles the target distribution [35]. The advantage of this domain mapping approach is that labels are not required for both the source and target domains. Thus, image-to-image translation is not affected by the label qualities or granularity differences of the classes defined by the labels.

Many studies using UDA have recently been conducted on remote sensing images [36], [37], [38], [39], [40]. These studies primarily focused on urban areas and employed publicly available datasets [36], [40], [41]. The most common knowledge transfer is a domain adaptation applied to semantic segmentation for land use land classification, which plays a major role in understanding local statistics [37], [38]. In addition, the latest research is focused on specific remote sensing problems, such as change detection, crop monitoring, and vehicle detection [42], [43], [44]. These new architectures proposed complicated concepts including multisource/ multitarget adaptation, and statistical domain alignment techniques [35], [36], [39]. Whereas the tailored model can achieve very good performance in certain conditions, this framework makes it difficult to extend its performance to different conditions or scenarios.

While the final goal of this study is to characterize the marine debris distribution in coastal areas, our focus in UDA is on the knowledge transfer of semantic segmentation models. The biggest challenge in our study is to transfer information about marine debris using UDA, which has not been explicitly trained for this particular application. The spatial representation
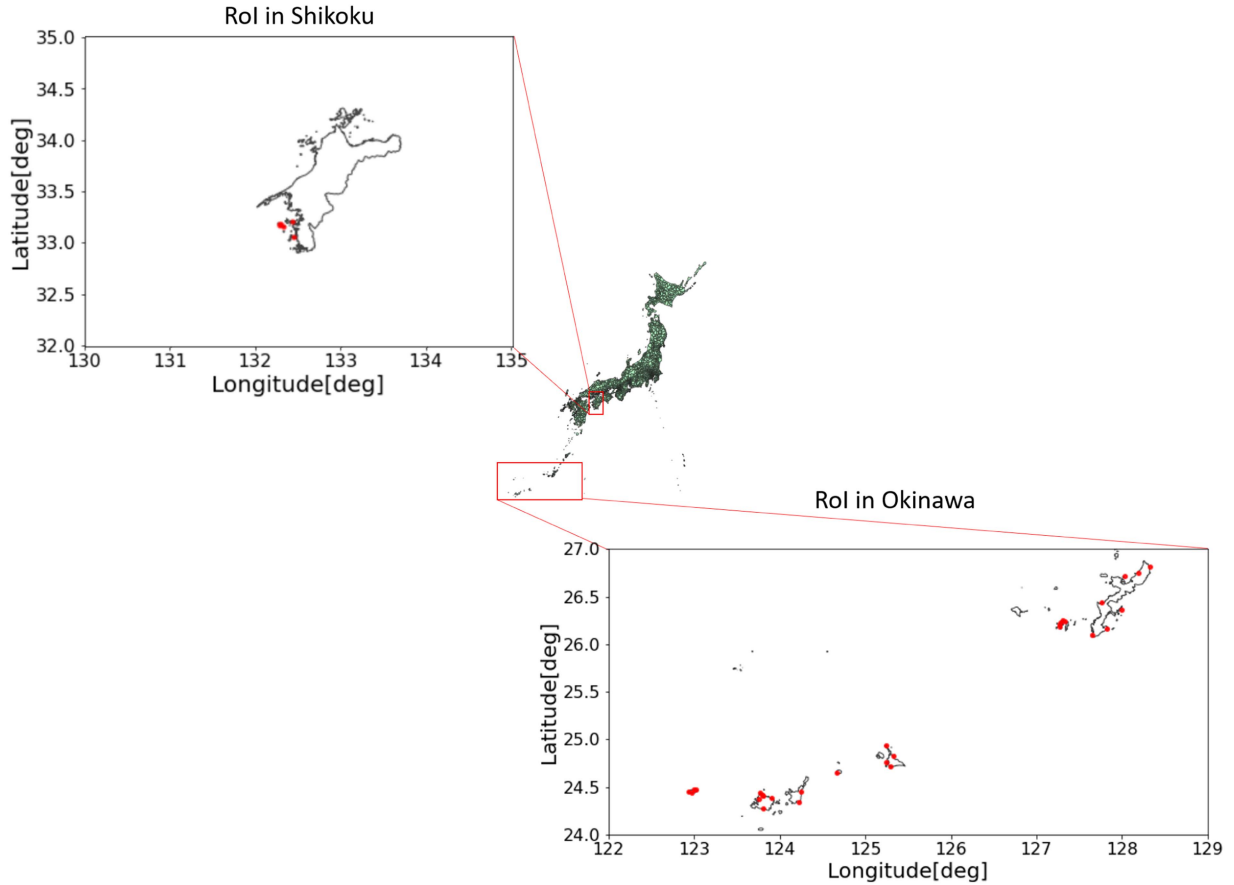
Fig. 1. Targets of interest located in Okinawa: Southeast islands in Japan and Shikoku: inland sea of Japan. Red dots show the cleanup beach locations.

of beach debris at subpixel scales is complicated due to the significant variability in its components and backgrounds. The beach itself can consist of various types of sand, mud, and vegetation. Meanwhile, the scattered debris encompasses different materials with varying orientations, influenced by tides, currents, and meteorological events, such as typhoons. Hence, the primary objective of this study is to evaluate the ability of UDA to effectively characterize coastal marine debris under various conditions. We have assumed two general transfer scenarios that account for the major differences in debris characterization as follows. 1) Transferring the model developed for high spatial resolution satellite images to lower resolution satellite images. 2) Applying the classification results from data-rich environments to areas with far fewer high-resolution satellite images.

II. STUDY AREA AND DATASET

As we mentioned in Section I, we need two different sites to perform our UDA. The first source location is Okinawa; the same site used in the previous study [30], and the new geographic region with fewer images is Shikoku Island, a beach of a Japanese inland sea shown in Fig. 1. This region and the Okinawa region have dramatically different climates in Koppen's climate classification [45], which results in differences in the local characteristics especially in vegetation and general

TABLE I
SATELLITE IMAGERY SPECIFICATIONS

Satellite	Band	Spatial res.[m/pix]	Temporal res.	# of sat
WorldView-2,3	8	0.46, 0.31	daily	2
Pleiades	4	0.5	daily	2
Skysat	4	0.7	12 visits/day	21

background, as shown in Fig. 2. We analyzed the following satellite data at these locations.

1) WV Okinawa dataset (42 scenes).
2) Pleiades Okinawa dataset (27 scenes).
3) Skysat Okinawa dataset (four scenes).
4) Skysat Shikoku dataset (three scenes).

We show the basic specification of three satellite image types in Table I. "Res." and "Sat" represent resolution and satellite, respectively.

We should note that all of the satellite images have submeter spatial resolution and the data are acquired from the archive data. The temporal resolutions presented in Table I apply to new capture requests, while the archived dataset is available approximately on a weekly basis for WorldView and Pleiades images, and daily for Skysat images. It should be noted that the data acquisition may be significantly reduced due to cloud cover, which is dependent on local weather conditions. In our region of interest, the actual data acquisition rate was approximately

Fig. 2. Example of debris on target locations in southern islands of Japan (Left) and Shikoku area (Right) where fewer samples are available. We can observe the background difference (vegetation and sand) due to the weather conditions. Debris tends to deposit from the middle to the "high water mark" of the beach rather than at the ocean shoreline.

2–3 times per month for WorldView and Pleiades, and once per week for Skysat images.

A UDA analysis that utilizes such widely used satellite data yields an important method to increase the sampling frequency. All images we obtained are pansharpened L2 surface reflectance (SR) products. These images contained urban structures, vegetation, mountains, and coastal regions. We selected nine classes (vegetation, trees, buildings, roads, manmade structures, water, sand, rocks, and others) to cover the diversity of elements contained in these images. We prepared the labeling of 202 km^2 of Maxar WorldView images, 178 km^2 of Pleiades images, and 544 km^2 of Planet Skysat images for the Okinawa area. The overall WorldView and Pleiades dataset is comprised of 42 and 27 scenes, respectively, with smaller areas whereas the Skysat dataset is only four scenes. Although the entire area of Skysat is larger than that of WorldView or Pleiades, the variability including radiometric difference is much larger in WorldView and Pleiades data. Total beach sites in their datasets result in 49, 32, and 13 samples to be analyzed, respectively.

As for the Shikoku dataset, we only have three images, which result in 9.3 km^2 covering 616 tiles. The latter small dataset is ideal for the few-shot domain adaptation. We show both regions of interest in Fig. 1

To preprocess the images, we split them into small patches of 224×224 pixels with no overlap. This results in 1.61×10^4 tiles for WorldView, 4.33×10^4 tiles for Skysat and 1.42×10^4 tiles for Pleiades. All of our processing steps are carried out in these patches.

A. In-Situ Measurement

We collected local information from the two aforementioned regions. In Okinawa, the target beaches undergo regular cleanup every few months to maintain their appeal to the tourists industry. The clean-up operation is manually conducted and collected debris is classified into different categories and measured as weight and volume. The detailed log was made in 50-m bands across the beach. These clean-up operations have been going on since 2014. For our study, we selected 29 beaches to be analyzed,

each of which has a different length and width and occur on different islands, as shown by the red dots in Fig. 1.

On the other hand, the beaches in the Shikoku region do not undergo regular cleanup operations, resulting in a higher accumulation of debris compared to the cleaned beaches in Okinawa. The ground truth data in Shikoku relies solely on visual estimates conducted by local investigations. Moreover, access to these areas is challenging due to their terrain. Therefore, we can assume that the debris accumulation in these areas is primarily influenced by natural processes, with minimal human intervention.

In this analysis, we used the total volume of the debris and the debris value is normalized by the length of the beach. A relatively clean beach has a value of 10 L/50 m while a dirty beach will have a value of 5000 L/50 m, which corresponds to the left image shown in Fig. 2. These normalized values serve as indicators of the debris level present on the beach. Further details regarding the acquisition and processing of the ground truth data can be found in our previous studies [30].

III. METHODOLOGY

We summarize our analysis in Fig. 3. The estimate of marine debris is conducted based on the entropy calculated by the semantic segmentation model. The analysis procedure is described in more detail in the previous study [30]. The entropy as defined in (1) provides a probabilistic metric to quantify the inhomogeneity on the beaches [46] and we found that it has a high correlation with the amount of debris accumulation. Therefore, we need to extract the accurate sand area using our segmentation model and calculate the entropy from the output. We used the U-net model for the segmentation as in the previous analysis

$$H_s^{(h,w,c)} = -\sum_{c \in C} p_s^{(h,w,c)} \log p_s^{(h,w,c)}. \tag{1}$$

Our UDA approach is a two-step process, illustrated in Fig. 3; to perform image-to-image translation using the CycleGAN technique [34]. This step focuses on adapting the images from
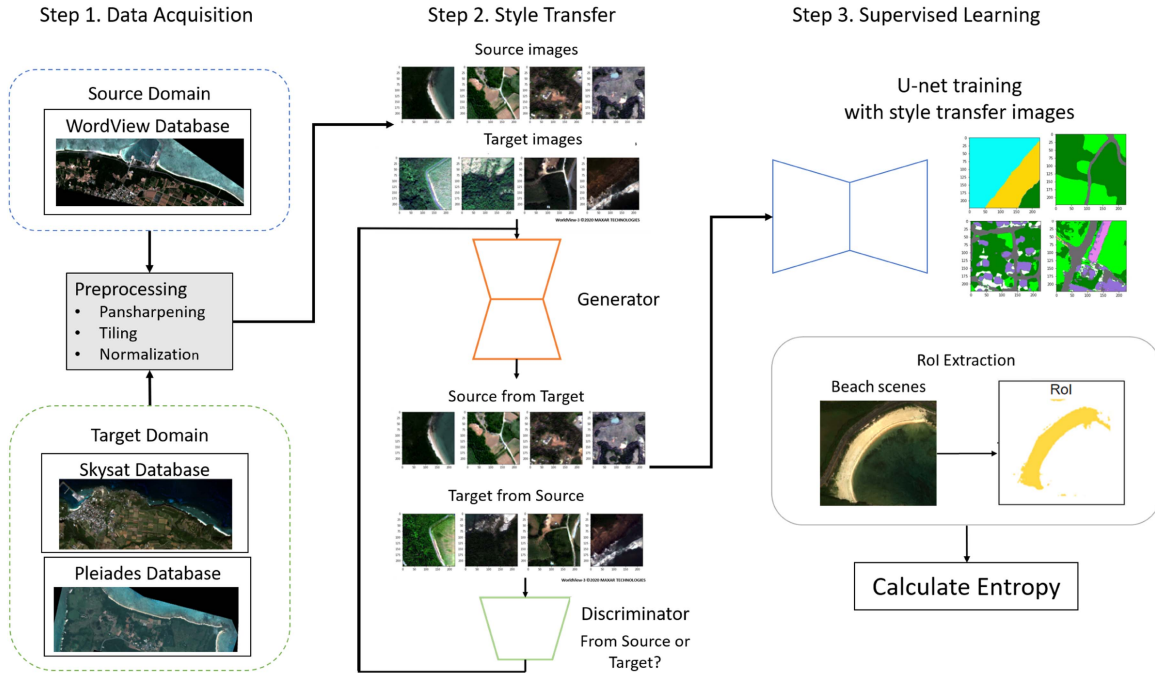
Fig. 3.   Our image data processing pipeline from data acquisition of multiple satellite images to the debris characterization using UDA. (Original satellite images from WorldView-3 ©2023 MAXAR TECHNOLOGIES, Pleiades ©Airbus, and Skysat ©Planet).

the source domain (e.g., MAXAR WorldView) to align with the target domain (e.g., Planet Skysat), and to train a U-net model for segmentation using translated images. We conducted two UDA cases to address different scenarios. The first case transferred the model developed for Okinawa, utilizing a large number of WorldView images, to lower-resolution satellite images, such as Skysat. For this case, we employed CycleGAN. The second case involved applying the classification results obtained from the data-rich environment of Okinawa to an area with a significantly lower number of satellite images. In this case, we utilized CycleGAN with cross-domain correspondence.

A. CycleGAN

CycleGAN is frequently utilized for image style transfer [34] and was originally proposed for image-to-image translation known as "pix2pix" transformation [47]. CycleGAN uses a convolutional neural network that employs a conditional adversarial generative network [48] without using paired images during the training. CycleGAN constructs a mapping function $G : X \rightarrow Y$ such that the output images $G(X)$ are projected within the distribution of images Y using adversarial loss as a criterion. This framework also adds another mapping constraint with inverse mapping. CycleGAN is employed with a cycle consistency loss to enforce $F(G(X)) \approx X$. This adversarial loss with the cycle consistency is known to achieve image generation with very high quality in various contextual shifts [34].

B. Cross Domain Correspondence

It is generally not possible to have a large number of high-resolution satellite images at each debris site. Consequently,

it is important to develop a UDA approach that can perform effectively even with a small number of images.

To address this issue, we introduced the concept of cross-domain correspondence [49] into the CycleGAN architecture. By incorporating this additional constraint, we aim to compensate for the data variability in the satellite data. We benefited from previous studies on "few-shot image generation" [50], [51], which focus on preserving the diversity of data transformations during the knowledge transfer phase. The overfitting during the transfer phase results in the difference in relative distances of samples in the source domain and transfer domain [50]. Therefore, the preservation of relative pairwise distances will help prevent overfitting and collapsed image generation.

To implement the concept of cross-domain distance consistency [50], we calculated the cross-domain distance by comparing the similarity between data samples in two domains. Unlike the traditional images used in previous studies, satellite images have complex spatial representations, making it challenging to achieve precise domain alignment with only a few images. The generator in CycleGAN has an encoder–decoder architecture and the features computed by the encoder can be represented as high-dimensional features. Therefore, we computed the cross-domain distance using the retrieved features in CycleGAN. The images: x_i are encoded in the generator as $E(x_i)$ using the encoder E. Initially, we estimated data diversity by evaluating the similarity between the generated images x_i in the feature space from a large source dataset $\mathcal{D}_s$ using the cosine similarity function sim() shown in (2) as follows. Here, E_s represents the encoder of the generator G_s, and the subscripts s and t indicate the source and target domains, respectively. Subsequently, we calculated the cross-domain distance $\mathcal{L}_{\text{dist}}$ using the

TABLE II
TILED DATASET LIST

Dataset	# of tiles
WV Okinawa	2542
Pleiades Okinawa	2950
Skysat Okinawa	4345
Skysat Shikoku	319

TABLE III
PARAMETER LIST FOR UDA ANALYSIS

Parameters	UDA of different sat. images	Few-shot UDA
Batch size	1	4
Epoch	200	1
λ	–	10 000

Kullback–Leibler (KL) divergence as defined in (3) as follows. KL divergence quantifies the difference between two probability distributions [52]. It characterizes the relative pairwise distance between the two domains. Therefore, $\mathcal{L}_{\text{dist}}$ penalizes the GAN model to maintain the relative distance distribution of sampled images.

As a consequence, the model preserved the variance of the generated images even after being updated with the target domain data. Therefore, the model was updated by integrating the CycleGAN loss ($\mathcal{L}_{\text{cyc}}$) and cross-domain distance loss ($\mathcal{L}_{\text{dist}}$), as given in (4). A significant advantage of this approach is that it can be simply added to the loss function without updating the GAN architecture, allowing the use of any model for a dataset with a small number of samples. We refer to this architecture as a "few-shot" model

$$y_i^s = \text{Softmax}\left(\{\text{sim}\left(E_s\left(x_i\right), E_s\left(x_j\right)\right)\}_{\forall i \neq j}\right)$$

$$y_i^{s \to t} = \text{Softmax}\left(\{\text{sim}\left(E_{s \to t}\left(x_i\right), E_{s \to t}\left(x_j\right)\right)\}_{\forall i \neq j}\right) \quad (2)$$

$$\mathcal{L}_{\text{dist}}\left(G_{s \to t}, G_s\right) = \mathbb{E}_{\{x_i \sim \mathcal{D}_t\}} \sum_i D_{KL}\left(y_i^{s \to t} \| y_i^s\right) \quad (3)$$

$$G_{s \to t}^* = \arg \min_G \max_{D_{\text{patch}}} \mathcal{L}_{\text{cyc}}\left(G, D_{\text{patch}}\right)$$
$$+ \lambda \mathcal{L}_{\text{dist}}\left(G, G_s\right). \quad (4)$$

IV. EXPERIMENTAL STUDY

We conducted statistical analyses using the aforementioned data and models using the detailed settings given below. We first prepared the tiled images for each dataset, as described in Table II. We did not use all of the tiles but rather chose the tiles that contained more than one class since the majority of tiles contained only "water" or "trees." This resulted in roughly 2500, 3000, and 4300 tiles for the Okinawa WV dataset, the Pleiades dataset, and the Skysat dataset, respectively. In addition, we calculated the class intersection over union (IoU) to test the accuracy of our model for each case.

A. Algorithm

We examined other domain adaptation architectures to compare with our CycleGAN model. First, we examined a U-net model [53] trained with supervised learning. We, then, implemented the CycleGAN and other similar domain adaptation algorithms: adversarial entropy minimization (AdvEnt) [54], FDA [55] and CyCADA [56].

AdvEnt is based on adversarial training, which uses the label information. The entropy values are high when the model dictates that the images are not well aligned with the training data. Thus, AdvEnt minimizes entropy by ensuring that the entropy distribution of the target domain aligns with that of the source domain [54]. By aligning the entropy distributions, AdvEnt enhances both the consistency and similarity between the segmentation maps of different domains. We used this algorithm because the direct adaptation of the entropy metric was also effective for our debris study as well.

Fourier domain adaptation (FDA) is also a straightforward approach for reducing the distribution discrepancy between the source and target domains by swapping their low-frequency spectra [55] with that of the source domain. This method does not require any training of the model but instead uses a Fourier transform. The low-frequency domain captures large-scale features that are typically the major reasons for discrepancies between the different image domains.

Cycle-consistent adversarial domain adaptation (CyCADA) [56], is similar to CycleGAN but also incorporates a training phase for segmentation. This method combines cycle consistency, semantic consistency, and adversarial objectives to generate a final target model [56]. Semantic consistency aims to measure the difference in spatial representation before and after the image translation. It is computed by comparing the labels from the source domain with the segmentation output obtained using the style-transferred images.

B. Application of UDA to Different Satellite Images

As is clear from Table I, Skysat images are quite different from WorldView images in terms of spatial and spectral resolutions. We utilized four bands from the WorldView images that closely matched those of Skysat (Pelaides) and performed the UDA process. The parameters employed in our studies are summarized in Table III. An important advantage of CycleGAN is its ability to perform style transfer without the need for pairwise images, allowing us to conduct the transfer using varying numbers of tiles in each domain. However, it is necessary to run this style transfer process for a sufficient number of epochs to accurately represent the images in the target domain, which requires a large number of iterations and high computational costs. We also monitored the training loss functions for both discriminators and generators shown in Fig. 4. Steady decreases in both losses were observed. Notably, the discriminator's loss increased toward the end of training, which suggests that the generator was producing increasingly convincing images capable of fooling the discriminator.

C. Application to Small Sample Conditions

We also wanted to test the UDA as applied to the case with a few samples. As we mentioned in Section II, we have only
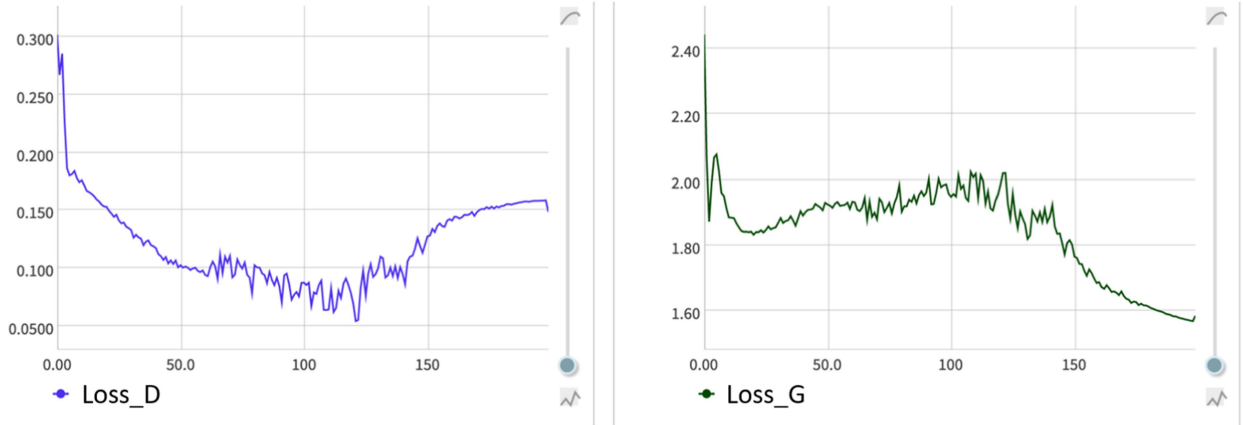
Fig. 4.   Training loss curves of CycleGAN for style transfer from Worldview to Skysat images: the discriminator's loss (Loss_D)(left plot (blue)), the generator's loss (Loss_G)(right plot (green)).

TABLE IV
CLASS IoU OF INFERENCE RESULT USING SKYSAT IMAGES BY DIFFERENT UDA MODELS

IoU	Others	Vegetation	Trees	Building	Roads	Manmade structure	Water	Sand/dirt	Rocks	All
Skysat (supervised)	0	0.733	0.769	0.288	0.32	0.007	0.991	0.393	0.402	0.756
WorldView (direct transfer)	0	0	0.481	0.056	0	0.001	0.907	0.204	0.036	0.368
AdvEnt	0	0.194	**0.688**	0.058	0.02	0.04	**0.986**	0.346	0.059	0.478
FDA	0	0.001	0.503	0	0.016	0	0.906	0.238	0.033	0.375
CycleGAN	0.003	**0.634**	0.551	**0.145**	0.22	**0.069**	0.95	**0.30**	0.084	**0.661**
CyCADA	0	0.579	0.615	0	**0.224**	0.001	0.977	0.39	**0.201**	0.641

The bold values show the highest IoU scores achieved for each class category of features.

three Skysat images for the Shikoku area that is geographically very different from Okinawa and can be expected to have a very different spatial distribution of debris in the satellite images. We run the UDA with the CycleGAN combined with cross-domain correspondence having the parameters shown in Table III. We should note that this style transfer is initialized with the Cycle-GAN model discussed in Section IV-B.

D. Correlation Analysis

We performed a correlation analysis using entropy derived from the UDA models and the ground truth "clean-up" data. We should note that the CycleGAN transfer from WorldView to Skysat (Pleiades) also generates the model from Skysat (Pleiades) to WorldView transfer model. Therefore, when you apply the UDA model for debris characterization, we can calculate the entropy in two ways: in the WorldView domain or in the Skysat (Pleiades) domain. The first method is to compute entropy from the worldview-styled Skysat (Pleiades) images using the segmentation model trained by the WorldView images. The second method is to compute entropy from Skysat images using the segmentation model trained by Skysat (Pleiades)-styled WorldView images.

E. Debris Estimation in Different Areas

We also analyzed the entropy in the Shikoku area using the few-shot UDA model. In this experiment, we only have six beaches and could not observe the correlation with the ground

truth data. Therefore, we present the result of entropy analysis for both clean and dirty cases.

V. RESULTS AND DISCUSSION

We will first present the result of our UDA models and then, we will discuss the statistical analyses for debris characterization.

A. Application of UDA to Different Satellite Images

The results for Skysat images are summarized in Table IV. To better visualize these comparisons, we plot them in Fig. 5. For comparison purposes, we also included the results of supervised learning models and other UDA approaches. As expected, the supervised learning models achieved the highest IoU scores, while the transfer learning models had lower IoU scores due to the associated domain shift. Qualitatively, the AdvEnt and FDA models exhibited inaccuracies in capturing the spatial distributions, resulting in some areas being misclassified. AdvEnt, in particular, exhibited higher accuracy in major classes. This can be attributed to the AdvEnt model's update mechanism, which aims to make the output of the target domain resemble that of the source domain. As a result, this model tends to prioritize the accurate representations of major classes while potentially sacrificing the finer details in the generated segmentation maps. In contrast, we can observe the improvement of Class IoU from the direct transfer learning model when we apply the CycleGAN
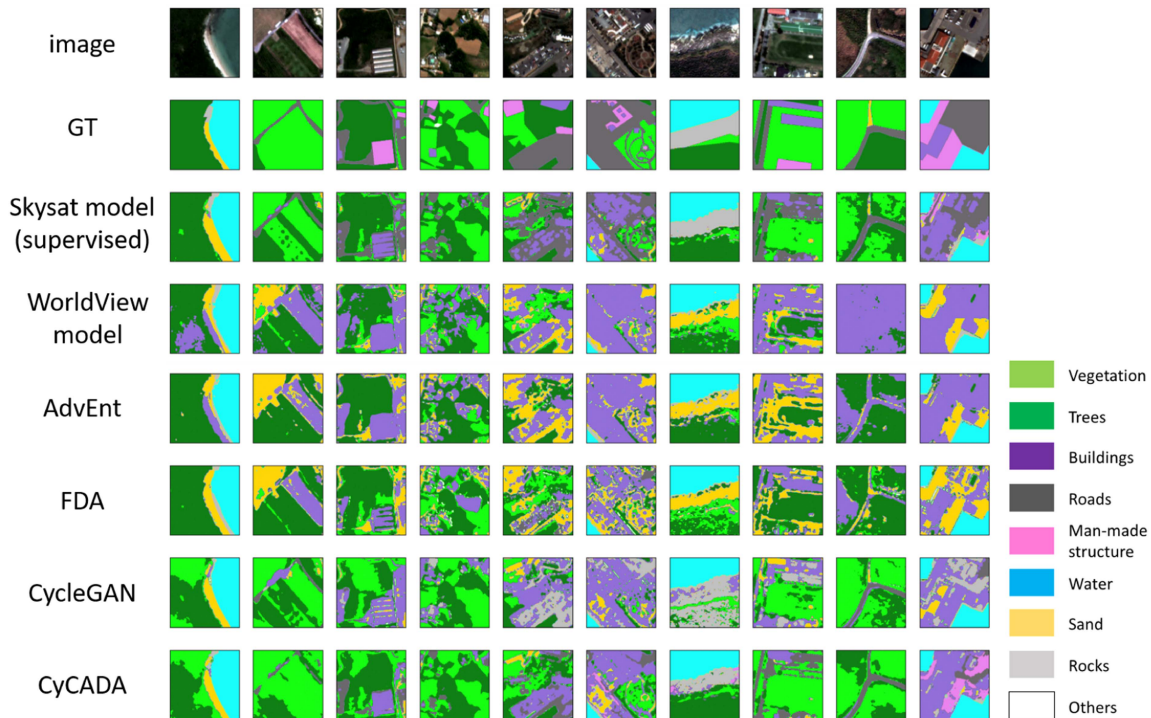
Fig. 5.　Inference result of tile images of Skysat for segmentation using UDA approaches (original satellite images from Skysat ©Planet).

TABLE V
CLASS IoU OF INFERENCE RESULT USING PLEAIDES IMAGES BY DIFFERENT UDA MODELS

IoU	Others	Vegetation	Trees	Building	Roads	Manmade structure	Water	Sand/dirt	Rocks	All
Airbus (supervised)	0.969	0.511	0.838	0.099	0.225	0.075	0.97	0.348	0.103	0.852
WorldView (direct transfer)	**0.99**	0.098	0.752	**0.302**	**0.27**	0.036	0.950	0.243	0.027	0.812
AdvEnt	0.982	0.508	0.805	0.2	0.172	**0.112**	0.91	**0.38**	0.025	0.829
FDA	0.969	0.482	0.754	0.043	0.012	0.026	0.949	0.304	0.011	0.803
CycleGAN	0.969	**0.552**	**0.812**	0	0.095	0	0.953	0.174	0.024	**0.842**
CyCADA	0.969	0.532	0.797	0.001	0.143	0	**0.955**	0.147	**0.037**	0.837

The bold values show the highest IoU scores achieved for each class category of features.

or CyCADA models. We should mention that the important capability of our segmentation model is an accurate segmentation of the minor classes (road, building, sand, etc.). The class IoU is greatly improved especially in vegetation, buildings, roads, manmade structures, and sand/dirt. These features are needed to characterize the presence of beach marine debris in our case. CyCADA achieved a more accurate extraction of minor classes as the architecture also incorporated the supervised training phase.

We also summarize the result for Pleiades images in Table V. We plot the inference tiles in Fig. 6 showing supervised learning models with other similar UDA models. Similar to the SkySat cases, supervised learning models achieved the highest IoU scores. However, the direct transfer model can also achieve good segmentation performance, reaching a total IoU of over 0.8. This is due to the similar specification between WorldView and Pleiades. WorldView-2 images, from which the majority of the WorldView dataset is cropped, and Pleiades images have roughly the same spatial resolution of 0.5 m/pix. Both types of images are SR products. The main difference of these two datasets is a preprocessing algorithm for pansharpening. Pleiades images are processed using the Airbus DS proprietary algorithm, whereas WorldView images are processed manually using public library algorithms. [57]. The fact that the direct transfer model has lower IoU in vegetation and tree classes than other UDA approaches may be due to the difference in the preprocessing algorithms. This suggests that the difference in preprocessing algorithms resulted in some changes in the segmentation accuracy. Other UDA approaches also achieve good performance as well in this study. CycleGAN and CyCADA, in particular, have superior performance to the other UDA approaches by 2–3 points in total IoU.

B. Application to Small Sample Conditions

The results of applying UDA to the small sample case are presented here in Table VI. To visually present this analysis,
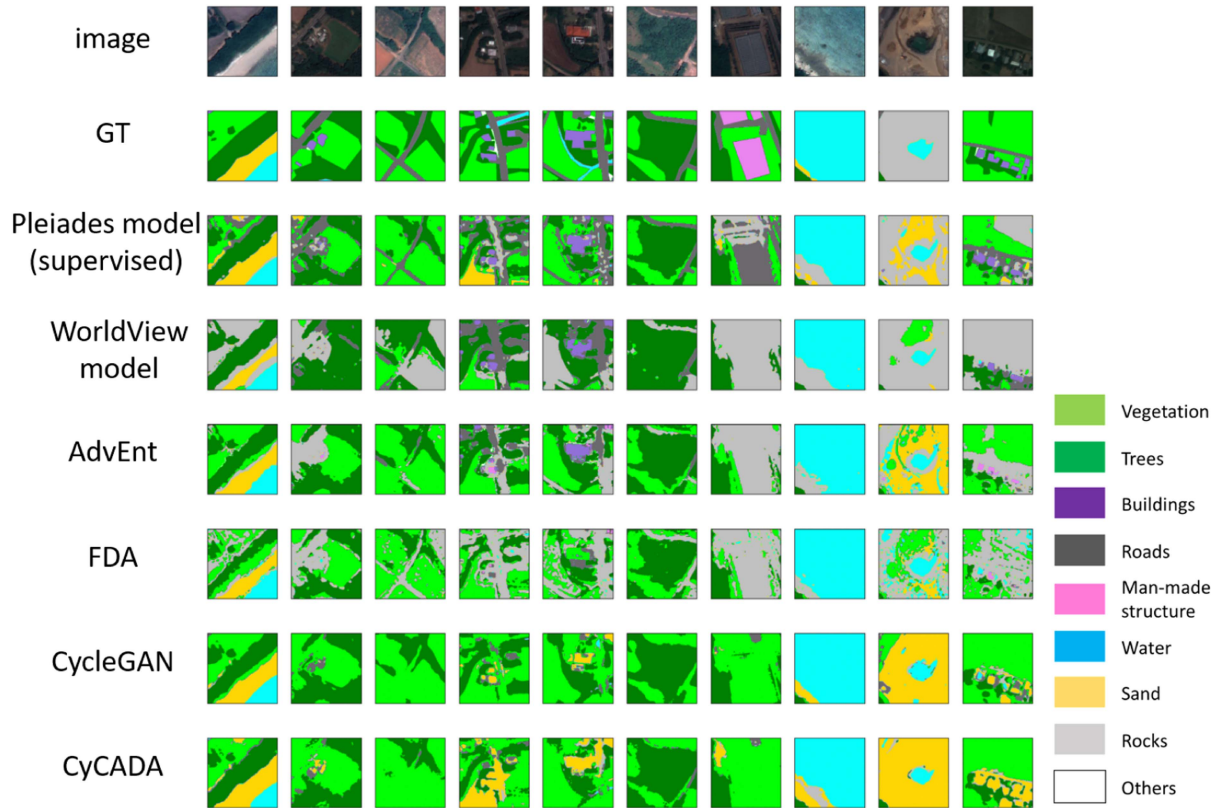
Fig. 6. Inference result of tile images of Pleiades for segmentation using UDA approaches (original satellite images from Pleiades ©Airbus).

TABLE VI
CLASS IoU OF INFERENCE RESULT USING SKYSAT IMAGES BY DIFFERENT UDA MODELS

IoU	Others	Vegetation	Trees	Building	Roads	Manmade structure	Water	Sand/dirt	Rocks	All
Skysat (supervised)	0	0.334	0.911	0.038	0.209	0	0.985	0.315	0.112	0.816
CycleGAN	0.003	0.105	0.891	**0.025**	0.022	**0.14**	0.948	**0.319**	0	0.792
Few shot CycleGAN	0	0.156	0.916	0	0.06	0.001	0.961	0.042	0.001	0.81
Few shot CyCADA	0	**0.227**	**0.929**	0	**0.359**	0	**0.976**	0.152	**0.043**	**0.831**

The bold values show the highest IoU scores achieved for each class category of features.

we plotted the results of the "few-shot UDA models in Fig. 7. In this scenario, even the supervised model does not do very well with the spatial classification, especially in the areas with multiple classes. This result indicates that supervised learning with small amounts of data could not retrieve the spatial patterns, especially in the minor classes. In the case of the CycleGAN model, the transfer to several Skysat images exhibits very poor accuracy. This can be attributed to the limited dataset and the difficulty of style transfer models in capturing detailed feature distributions. On the other hand, the few-shot CycleGAN and CyCADA models demonstrated improved performance, with smoother and consistent segmentation maps. The class IoU also showed significant improvements, as it produced highly accurate maps with IoU levels superior to those of the supervised model. Although the inference of few-shot CycleGAN and CyCADA has similar IoU values, CyCADA showed more robustness in the presence of the minor classes, such as road, sand, and rocks.

This is attributed to the use of semantic consistency loss, which compares the spatial distribution of the source image and style transferred image. The target images were only cropped near the coast, where the dominant semantics are ocean, road, sand, and rocks, while the CyCADA model captures the representation of these frequent occurring classes more efficiently than CycleGAN model.

C. Correlation Analysis

Here, we used the UDA model to calculate the entropy values in each location. We present the correlation plots in Figs. 8 and 9 for Skysat and Pleiades images, respectively. We computed the correlation coefficients and created the scatter plot with log-scaled debris values. These correlations are based on the fact that the area covered by debris on the beach will become saturated
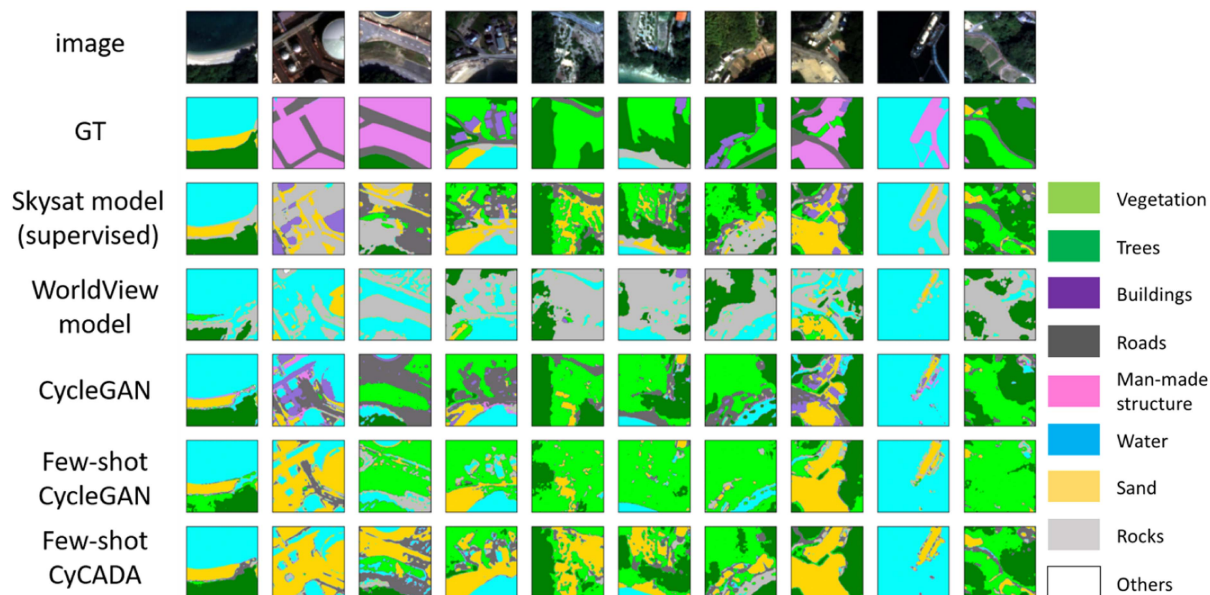
Fig. 7.   Inference result of tile images of Skysat for segmentation using few-shot UDA (original satellite images from Skysat ©Planet).
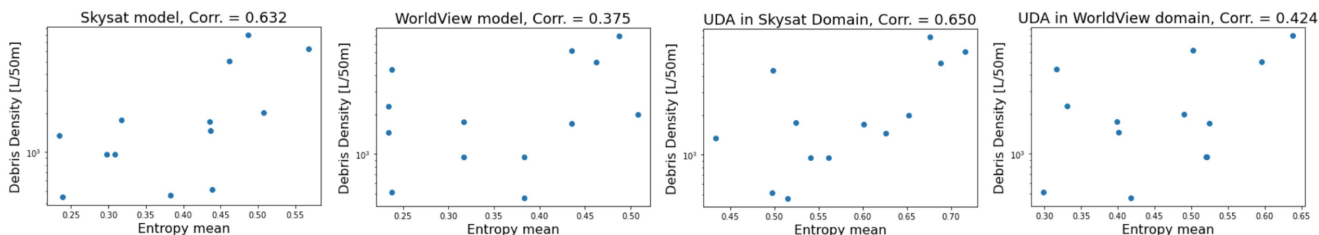

Fig. 8.   Correlation plots between debris density and entropy value of skysat images using different segmentation models: Skysat model (supervised) (left), WorldView model (2nd left), UDA model computed in Skysat domain (3rd left), and UDA model computed in WorldView domain (right).
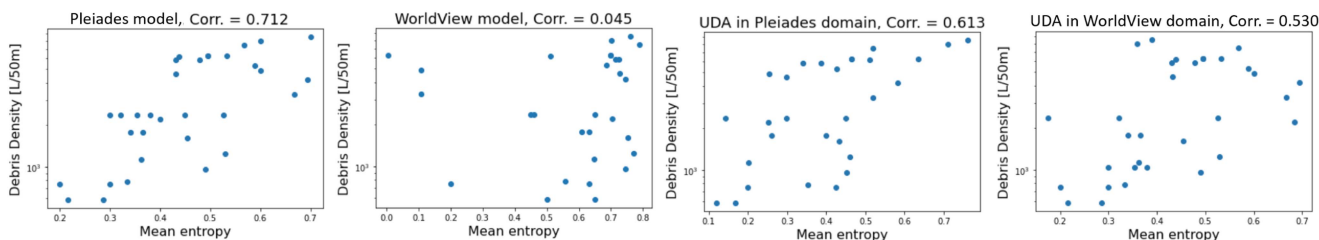

Fig. 9.   Correlation plots between debris density and entropy value of Pleiades images using different segmentation models: Pleiades model (supervised) (left), WorldView model (2nd left), UDA model computed in Pleiades domain (3rd left), and UDA model computed in WorldView domain (right).

as the area increases. We also show the examples of inference results in Figs. 10 and 11.

Overall trends are consistent both in Skysat and Pleiades cases. For instance, the correlation of the direct transfer learning model is very low as it does not generate accurate segmentation maps. Conducting UDA in the source domain tends to get a lower correlation than in the target domain.

In the case of Skysat images, we found that the correlation is the highest when the entropy is computed using the UDA model in the target domain. This is because the Skysat model was trained with a dataset, which does not include various capture conditions and beach sites. This results in a poor capability of acquiring the various beach or radiometric conditions. Also, the segmentation model tends to overfit the training data, leading to lower entropy values. In contrast, applying UDA to target images tends to cause an increase in entropy values overall. In this case, the source WorldView dataset has more variability in the images, which enables the UDA models to generate images with more abundant spatial representations than are found in the supervised models. In addition, it is known that UDA models
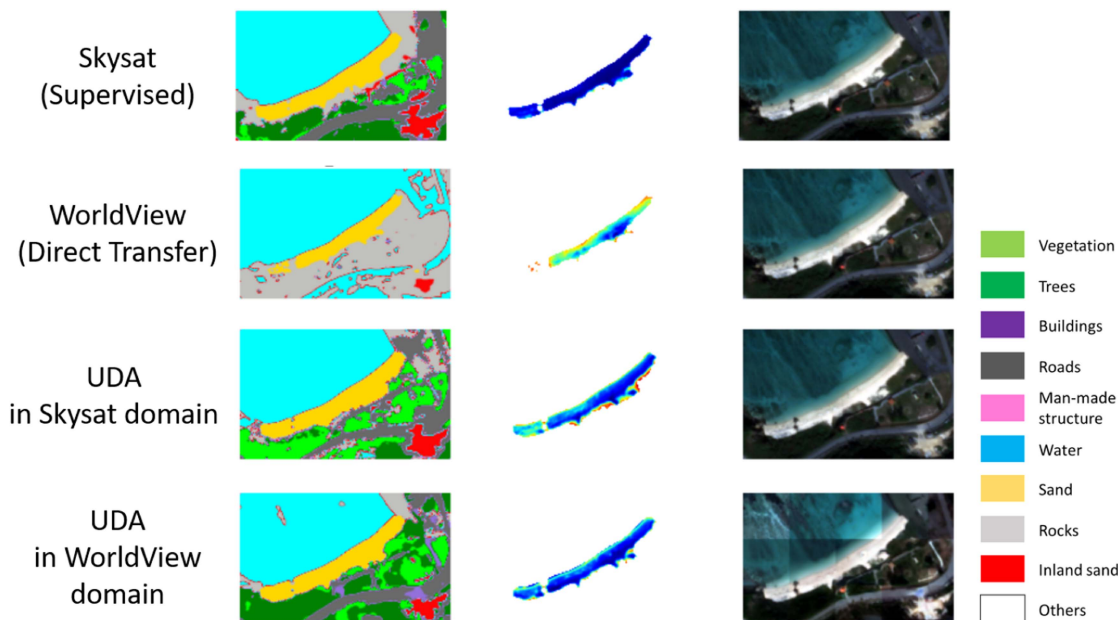
Fig. 10. Inference example of a target beach using different segmentation models (original satellite images from Skysat ©Planet). Left column shows segmentation maps, middle column shows entropy intensity maps and right column shows the satellite images.
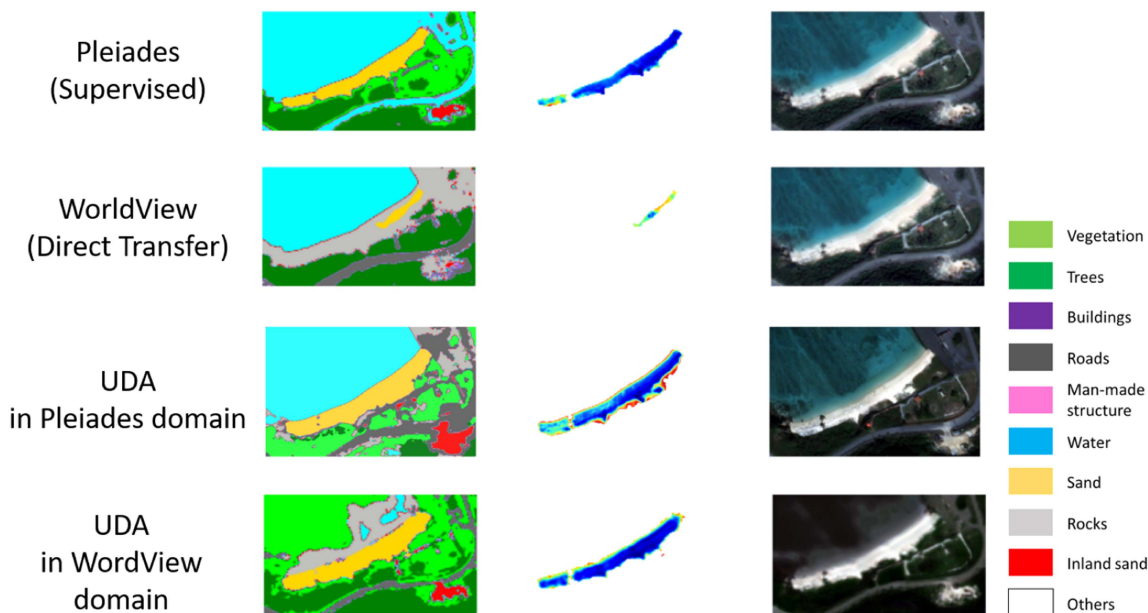

Fig. 11. Inference example of a target beach using different segmentation models (original satellite images from Pleiades ©Airbus). Left column shows segmentation maps, middle column shows entropy intensity maps, and right column shows the satellite images.

trained in the target domain tend to achieve higher segmentation accuracy [58], [59]. This phenomenon explains why the correlation reached its highest value when computed for the Skysat images. This indicates a strong alignment between the UDA model and the target domain. We also note that using UDA in the WorldView domain results in nonhomogeneous images, as they are reconstructed from the tiles of the translated images. This can introduce variations that are inconsistencies in

the characteristics of the generated images, which influences the entropy calculation.

In the case of Pleiades images, the supervised learning model achieves the highest correlation as the Pleiades dataset exhibits greater variability, which enables the models to capture different beach conditions. UDA in the Pleiades domain is also capable of achieving a correlation coefficient of greater than 0.6 when compared with ground observations. We should note that the

Fig. 12. Inference example of a target beach compared with in-situ observation (Left: entropy map, middle: RGB image right column shows the satellite images from Pleiades ©Airbus Right: Cleanup records in each 50-m band).

TABLE VII
LIST OF COMPUTED ENTROPY AND GROUND TRUTH DATA

Ground truth [L/50m]	Entropy mean
2.67×10^2	0.655
3.05×10^2	0.638
3.75×10^2	0.654
1.15×10^3	0.681
1.16×10^5	0.811
2.71×10^6	0.832

correlation coefficient using the direct transfer model is very low, despite the fact that the segmentation accuracy is almost comparable to the supervised model. The WorldView model tends to generate higher entropy values than the Pleiades model. Therefore, this result indicates that high compatibility in the segmentation model does not necessarily translate to the effective transfer of debris information. We can also observe that the correlation of the Pleiades model is higher than that of Skysat due to the higher spatial resolution.

The inference results in Figs. 10 and 11 also show that the higher entropy resides on the inner side of the beach, which coincides with the conclusion found in the previous study [30]. To further investigate the debris representation of the entropy map, we visualized a comparison of the entropy map with in-situ observations in Fig. 12. We can see a good agreement between the cleaned debris amount and estimated entropy values. Although the entropy tends to be high along the boundaries of the semantics (e.g., ocean and sand), The area with consistent entropy increase coincides with the presence of marine debris.

Therefore, we demonstrated the ability to detect marine debris using Planet Skysat and Airbus Pleiades images, effectively increasing the sampling frequency from monthly to weekly, or even daily. This enhancement is achieved through the higher revisit rates of satellite constellations and by avoiding the acquisition of data obscured by clouds.

D. Debris Estimation in Different Areas

We also present the computed mean entropy values along with their respective ground truth data for Shikoku in Table VII. In addition, we provide examples of inference results from the Shikoku dataset in Fig. 13. In comparison to the debris analysis

conducted for Okinawa, as shown in Figs. 8 and 10, the overall entropy values in the Shikoku dataset are notably higher. This can be attributed to three primary factors as follows.

1) The beaches in the Shikoku region primarily consist of rocks and pebbles, which introduce greater heterogeneity and result in higher entropy values.
2) The number of available images used in this analysis is considerably smaller, leading to increased uncertainty in the segmentation output.
3) The presence of a higher amount of debris in this region increases the heterogeneity due to the absence of regular cleanup activities.

We calculated the entropy value where the segmentation class is classified as "roads" and "rocks" in this study. This is because the extracted beach areas primarily fall under these classes, which is the proper result as concrete and rocks exhibit similar spectral characteristics [60]. Despite the variability of entropy values, a clear distinction can be observed between relatively clean beaches and heavily polluted beaches. The dirtiest beach, depicted in the bottom left image of Fig. 13, exhibits significantly higher debris deposition and consequently presents a much higher overall entropy value. This particular beach, shown in the right image of Fig. 2, had debris accumulation in multiple layers, intertwined with adjacent grass.

It is important to note that the composition of marine debris in the Shikoku region predominantly consists of fishing components, whereas in Okinawa, it is comprised of various materials. Despite this difference in debris type, we found that the entropy method used for estimation is not significantly affected. This is because entropy captures the uncertainty of the probabilistic distribution, which is independent of the specific debris composition.

As a result, we demonstrated the debris detection model's adaptability to areas with limited samples, significantly reducing data acquisition costs and facilitating rapid assessment across various coastal regions.

VI. FUTURE WORK

In our study, we have demonstrated the feasibility of using the UDA model for marine debris characterization on beaches viewed with different types of satellite data and from a data-rich
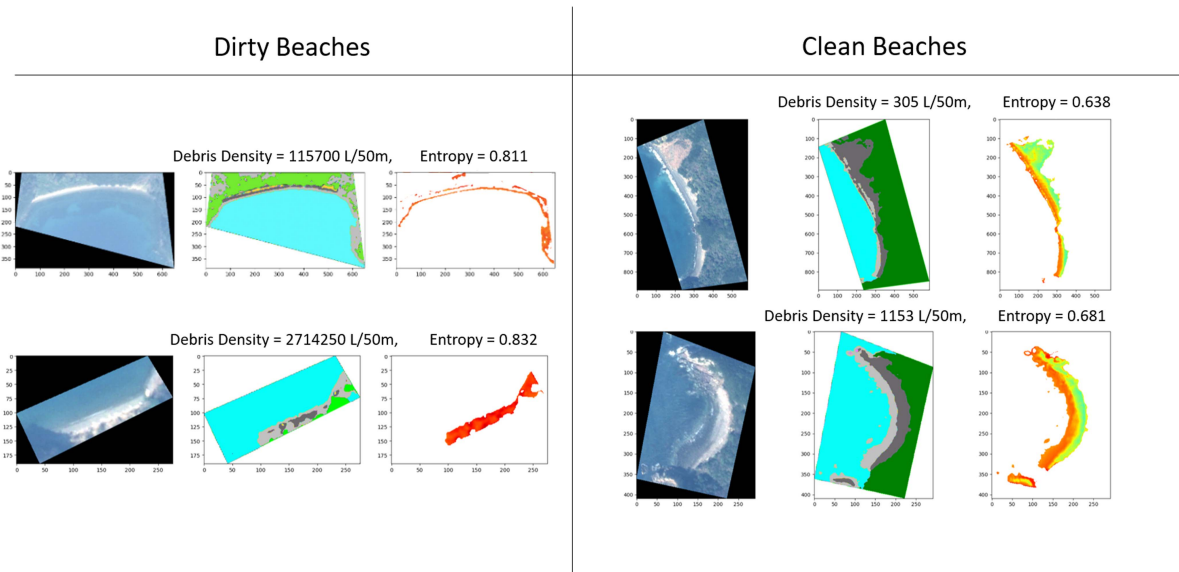
Fig. 13. Inference examples of target beaches in Shikoku using different segmentation models (original satellite images from Skysat ©Planet). Left column shows segmentation maps, the middle column shows entropy intensity maps and right column shows the satellite images. Each color represents the semantic class defined in the labels (Light green: vegetation, Green: trees, Purple: buildings, Dark gray: roads, Pink: other manmade structures, Light blue: water, Yellow: coastal sand, Gray: rocks, White: others, Red: inland sand).

region to one poor in satellite data coverage. However, further detailed analysis is necessary to provide a more comprehensive understanding of its capabilities and potential applications.

First, a time series analysis can be performed to visualize the temporal evolution of marine debris deposition. Employing our UDA model, we can utilize multiple satellite sensors for an enhanced characterization of marine debris. A detailed examination of the variations in debris deposition can reveal temporal or spatial patterns of increase and decrease. Such an analysis facilitates the correlation of meteorological events with fluctuations in debris deposition, potentially aiding in the prediction of debris arrival onshore.

Another further analysis is to explore and characterize the specific biases present in satellite images in greater detail. This includes examining the impact of preprocessing techniques, such as atmospheric correction and pansharpening, as well as accounting for geographical and sensor differences. Having prior knowledge of these influences will facilitate the implementation of UDA models for similar cases. Understanding and mitigating these biases will enhance the accuracy and reliability of our approach when applied to different datasets and scenarios.

Finally, while our current analysis is based on Japanese beaches due to in-situ data accessibility, it is important to acknowledge the potential applicability of our method to other similar beaches worldwide. Conducting a comparative analysis across geographically different regions will enable us to assess the ability to generalize our model to more diverse coastal environments.

VII. CONCLUSION

We developed robust debris estimation models using very high-resolution satellite images for practical assessment scenarios. We employed UDA, specifically utilizing the CycleGAN framework, to transfer the model trained using WorldView satellite images to other satellite sensors, such as Skysat and Pleiades. We tested two different scenarios and showed that this framework can improve the segmentation accuracy from World-View to Skysat/Pleiades images and from data-rich models to beaches with poor satellite coverage. We conducted statistical analyses and demonstrated the high correlation between the ground truth data and entropy metrics, which were computed using our UDA models. We also confirmed the good alignment of spatial debris estimation using entropy metrics and the actual collected debris records. This framework compensates for the differences in domains between the training dataset and the target dataset. Our approach enhances the sampling frequency of satellite images and facilitates rapid estimation, thereby proving to be an invaluable tool for coastal debris characterization and assessment.

REFERENCES

[1] A. A. Keller, E. L. Fruh, M. M. Johnson, V. Simon, and C. McGourty, "Distribution and abundance of anthropogenic marine debris along the shelf and slope of the us west coast," *Mar. Pollut. Bull.*, vol. 60, no. 5, pp. 692–700, 2010. [Online]. Available: https://www.sciencedirect.com/science/article/pii/S0025326X09005086

[2] C. Zhang, H. Zhou, Y. Cui, C. Wang, Y. Li, and D. Zhang, "Microplastics in offshore sediment in the yellow sea and east China sea, China," *Environ. Pollut.*, vol. 244, pp. 827–833, 2019. [Online]. Available: https://www.sciencedirect.com/science/article/pii/S0269749118336017

[3] Z. Zhang, H. Wu, G. Peng, P. Xu, and D. Li, "Coastal ocean dynamics reduce the export of microplastics to the open ocean," *Sci. Total Environ.*, vol. 713, 2020, Art. no. 136634. [Online]. Available: https://www.sciencedirect.com/science/article/pii/S0048969720301443

[4] F. Thevenon, C. Carroll, and J. Sousa, "Plastic debris in the ocean: The characterization of marine plastics and their environmental impacts, situation analysis report," Int. Union Conservation Nature, Gland, Switzerland, Tech. Rep., 2014. [Online]. Available: https://portals.iucn.org/library/node/44966

[5] I. Issifu and U. R. Sumaila, "A review of the production, recycling and management of marine plastic pollution," *J. Mar. Sci. Eng.*, vol. 8, no. 11, 2020, Art. no. 945. [Online]. Available: https://www.mdpi.com/2077-1312/8/11/945

[6] K. A. Boluk, C. T. Cavaliere, and F. Higgins-Desbiolles, "A critical framework for interrogating the united nations sustainable development goals 2030 agenda in tourism," *J. Sustain. Tourism*, vol. 27, no. 7, pp. 847–864, 2019, doi: 10.1080/09669582.2019.1619748.

[7] S. B. Sheavly and K. M. Register, "Marine debris & plastics: Environmental concerns, sources, impacts and solutions," *J. Polymers Environ.*, vol. 15, no. 4, pp. 301–305, 2007.

[8] G. Pasternak et al., "Nearshore survey and cleanup of benthic marine debris using citizen science divers along the mediterranean coast of Israel," *Ocean Coastal Manage.*, vol. 175, pp. 17–32, 2019. [Online]. Available: https://www.sciencedirect.com/science/article/pii/S0964569118308007

[9] S. Gall and R. Thompson, "The impact of debris on marine life," *Mar. Pollut. Bull.*, vol. 92, no. 1/2, pp. 170–179, Mar. 2015, doi: 10.1016/j.marpolbul.2014.12.041.

[10] A. Jain, B. N. Singh, S. P. Singh, H. B. Singh, and S. Singh, "Exploring biodiversity as bioindicators for water pollution," in *Proc. Nat. Conf. Biodiversity, Develop. Poverty Alleviation*, 2010, pp. 50–56.

[11] K. A. Owens, "Using experiential marine debris education to make an impact: Collecting debris, informing policy makers, and influencing students," *Mar. Pollut. Bull.*, vol. 127, pp. 804–810, 2018. [Online]. Available: https://www.sciencedirect.com/science/article/pii/S0025326X17308056

[12] I. E. Napper and R. C. Thompson, "Plastic debris in the marine environment: History and future challenges," *Glob. Challenges*, vol. 4, no. 6, 2020, Art. no. 1900081, doi: 10.1002/gch2.201900081.

[13] T. Aoyama, "Extraction of marine debris in the sea of Japan using high-spatial-resolution satellite images," in *Proc. SPIE Conf. Remote Sens. Oceans Inland Waters: Techn., Appl., Challenges*, 2016, vol. 9878, pp. 213–219, doi: 10.1117/12.2220370.

[14] K. Kylili, I. Kyriakides, A. Artusi, and C. Hadjistassou, "Identifying floating plastic marine debris using a deep learning approach," *Environ. Sci. Pollut. Res.*, vol. 26, no. 17, pp. 17091–17099, Jun. 2019, doi: 10.1007/s11356-019-05148-4.

[15] S. Kako, S. Morita, and T. Taneda, "Estimation of plastic marine debris volumes on beaches using unmanned aerial vehicles and image processing based on deep learning," *Mar. Pollut. Bull.*, vol. 155, 2020, Art. no. 111127. [Online]. Available: https://www.sciencedirect.com/science/article/pii/S0025326X20302459

[16] D. V. Politikos, E. Fakiris, A. Davvetas, I. A. Klampanos, and G. Papatheodorou, "Automatic detection of seafloor marine litter using towed camera images and deep learning," *Mar. Pollut. Bull.*, vol. 164, 2021, Art. no. 111974. [Online]. Available: https://www.sciencedirect.com/science/article/pii/S0025326X21000084

[17] T. Kataoka, C. C. Murray, and A. Isobe, "Quantification of marine macro-debris abundance around vancouver island, Canada, based on archived aerial photographs processed by projective transformation," *Mar. Pollut. Bull.*, vol. 132, pp. 44–51, 2018. [Online]. Available: https://www.sciencedirect.com/science/article/pii/S0025326X17307348

[18] L. Fallati, A. Polidori, C. Salvatore, L. Saponari, A. Savini, and P. Galli, "Anthropogenic marine debris assessment with unmanned aerial vehicle imagery and deep learning: A case study along the beaches of the republic of Maldives," *Sci. Total Environ.*, vol. 693, 2019, Art. no. 133581. [Online]. Available: https://www.sciencedirect.com/science/article/pii/S0048969719335065

[19] K. Moy et al., "Mapping coastal marine debris using aerial imagery and spatial analysis," *Mar. Pollut. Bull.*, vol. 132, pp. 52–59, 2018. [Online]. Available: http://www.sciencedirect.com/science/article/pii/S0025326X17310020

[20] G. Gonçalves, U. Andriolo, L. Pinto, and D. Duarte, "Mapping marine litter with unmanned aerial systems: A showcase comparison among manual image screening and machine learning techniques," *Mar. Pollut. Bull.*, vol. 155, 2020, Art. no. 111158. [Online]. Available: https://www.sciencedirect.com/science/article/pii/S0025326X20302769

[21] T. Acuña-Ruz et al., "Anthropogenic marine debris over beaches: Spectral characterization for remote sensing applications," *Remote Sens. Environ.*, vol. 217, pp. 309–322, 2018. [Online]. Available: https://www.sciencedirect.com/science/article/pii/S0034425718303730

[22] S. P. Garaba and H. M. Dierssen, "An airborne remote sensing case study of synthetic hydrocarbon detection using short wave infrared absorption features identified from marine-harvested macro- and microplastics," *Remote Sens. Environ.*, vol. 205, pp. 224–235, 2018. [Online]. Available: https://www.sciencedirect.com/science/article/pii/S0034425717305722

[23] K. Topouzelis, A. Papakonstantinou, and S. P. Garaba, "Detection of floating plastics from satellite and unmanned aerial systems (plastic litter project 2018)," *Int. J. Appl. Earth Observ. Geoinf.*, vol. 79, pp. 175–183, Jul. 2019.

[24] K. Topouzelis, D. Papageorgiou, A. Karagaitanakis, A. Papakonstantinou, and M. A. Ballesteros, "Plastic litter project 2019: Exploring the detection of floating plastic litter using drones and sentinel 2 satellite images," in *Proc. IEEE Int. Geosci. Remote Sens. Symp.*, 2020, pp. 6329–6332.

[25] K. Kikaki, I. Kakogeorgiou, P. Mikeli, D. E. Raitsos, and K. Karantzalos, "MARIDA: A benchmark for marine debris detection from sentinel-2 remote sensing data," *PLoS One*, vol. 17, no. 1, 2022, Art. no. e0262247, doi: 10.1371/journal.pone.0262247.

[26] A. Kikaki, K. Karantzalos, C. A. Power, and D. E. Raitsos, "Remotely sensing the source and transport of marine plastic debris in bay islands of Honduras (caribbean sea)," *Remote Sens.*, vol. 12, no. 11, 2020, Art. no. 1727. [Online]. Available: https://www.mdpi.com/2072-4292/12/11/1727

[27] C. Hu, "Remote detection of marine debris using satellite observations in the visible and near infrared spectral range: Challenges and potentials," *Remote Sens. Environ.*, vol. 259, 2021, Art. no. 112414. [Online]. Available: https://www.sciencedirect.com/science/article/pii/S0034425721001322

[28] L. Biermann, D. Clewley, V. Martinez-Vicente, and K. Topouzelis, "Finding plastic patches in coastal waters using optical satellite data," *Sci. Rep.*, vol. 10, no. 1, Apr. 2020, Art. no. 5364, doi: 10.1038/s41598-020-62298-z.

[29] H. Booth, W. Ma, and O. Karakuş, "High-precision density mapping of marine debris and floating plastics via satellite imagery," *Sci. Rep.*, vol. 13, no. 1, Apr. 2023, Art. no. 6822, doi: 10.1038/s41598-023-33612-2.

[30] K. Sasaki, T. Sekine, L.-J. Burtz, and W. J. Emery, "Coastal marine debris detection and density mapping with very high resolution satellite imagery," *IEEE J. Sel. Topics Appl. Earth Observ. Remote Sens.*, vol. 15, pp. 6391–6401, 2022.

[31] H. Wang et al., "Unsupervised domain adaptation for image classification via structure-conditioned adversarial learning," 2021, *arXiv:2103.02808*.

[32] G. Wilson and D. J. Cook, "A survey of unsupervised deep domain adaptation," *ACM Trans. Intell. Syst. Technol.*, vol. 11, no. 5, Jul. 2020, Art. no. 51, doi: 10.1145/3400066.

[33] W. Hong, Z. Wang, M. Yang, and J. Yuan, "Conditional generative adversarial network for structured domain adaptation," in *Proc. IEEE Conf. Comput. Vis. Pattern Recognit.*, 2018, pp. 1335–1344.

[34] J.-Y. Zhu, T. Park, P. Isola, and A. A. Efros, "Unpaired image-to-image translation using cycle-consistent adversarial networks," in *Proc. IEEE Int. Conf. Comput. Vis.*, 2017, pp. 2242–2251.

[35] O. Tasar, S. L. Happy, Y. Tarabalka, and P. Alliez, "ColorMapGAN: Unsupervised domain adaptation for semantic segmentation using color mapping generative adversarial networks," *IEEE Trans. Geosci. Remote Sens.*, vol. 58, no. 10, pp. 7178–7193, Oct. 2020.

[36] L. Zhang, M. Lan, J. Zhang, and D. Tao, "Stagewise unsupervised domain adaptation with adversarial self-training for road segmentation of remote-sensing images," *IEEE Trans. Geosci. Remote Sens.*, vol. 60, 2022, Art. no. 5609413.

[37] B. Benjdira, Y. Bazi, A. Koubaa, and K. Ouni, "Unsupervised domain adaptation using generative adversarial networks for semantic segmentation of aerial images," *Remote Sens.*, vol. 11, no. 11, 2019, Art. no. 1369. [Online]. Available: https://www.mdpi.com/2072-4292/11/11/1369

[38] Z. Zhang, K. Doi, A. Iwasaki, and G. Xu, "Unsupervised domain adaptation of high-resolution aerial images via correlation alignment and self training," *IEEE Geosci. Remote Sens. Lett.*, vol. 18, no. 4, pp. 746–750, Apr. 2021.

[39] J. Chen, J. Zhu, Y. Guo, G. Sun, Y. Zhang, and M. Deng, "Unsupervised domain adaptation for semantic segmentation of high-resolution remote sensing imagery driven by category-certainty attention," *IEEE Trans. Geosci. Remote Sens.*, vol. 60, 2022, Art. no. 5616915.

[40] M. Xu, M. Wu, K. Chen, C. Zhang, and J. Guo, "The eyes of the gods: A survey of unsupervised domain adaptation methods based on remote sensing data," *Remote Sens.*, vol. 14, no. 17, 2022, Art. no. 4380. [Online]. Available: https://www.mdpi.com/2072-4292/14/17/4380

[41] J. Iqbal and M. Ali, "Weakly-supervised domain adaptation for built-up region segmentation in aerial and satellite imagery," *ISPRS J. Photogrammetry Remote Sens.*, vol. 167, pp. 263–275, 2020. [Online]. Available: https://www.sciencedirect.com/science/article/pii/S0924271620301829

[42] B. Lucas, C. Pelletier, D. Schmidt, G. I. Webb, and F. Petitjean, "Unsupervised domain adaptation techniques for classification of satellite image time series," in *Proc. IEEE Int. Geosci. Remote Sens. Symp.*, 2020, pp. 1074–1077.

[43] Y. Wang, L. Feng, Z. Zhang, and F. Tian, "An unsupervised domain adaptation deep learning method for spatial and temporal transferable crop type mapping using sentinel-2 imagery," *ISPRS J. Photogrammetry Remote Sens.*, vol. 199, pp. 102–117, 2023. [Online]. Available: https://www.sciencedirect.com/science/article/pii/S0924271623000850

[44] P. J. Soto Vega et al., "An unsupervised domain adaptation approach for change detection and its application to deforestation mapping in tropical biomes," *ISPRS J. Photogrammetry Remote Sens.*, vol. 181, pp. 113–128, 2021. [Online]. Available: https://www.sciencedirect.com/science/article/pii/S092427162100232X

[45] M. C. Peel, B. L. Finlayson, and T. A. McMahon, "Updated world map of the Köppen-Geiger climate classification," *Hydrol. Earth Syst. Sci.*, vol. 11, no. 5, pp. 1633–1644, 2007. [Online]. Available: https://hess.copernicus.org/articles/11/1633/2007/

[46] J. Lin, "Divergence measures based on the Shannon entropy," *IEEE Trans. Inf. Theory*, vol. 37, no. 1, pp. 145–151, Jan. 1991.

[47] P. Isola, J.-Y. Zhu, T. Zhou, and A. A. Efros, "Image-to-image translation with conditional adversarial networks," in *Proc. IEEE Conf. Comput. Vis. Pattern Recognit.*, 2017, pp. 5967–5976.

[48] I. Goodfellow et al., "Generative adversarial nets," in *Proc. Int. Conf. Adv. Neural Inf. Process. Syst.*, 2014, vol. 27, pp. 2672–2680. [Online]. Available: https://proceedings.neurips.cc/paper/2014/file/5ca3e9b122f61f8f06494c97b1afccf3-Paper.pdf

[49] P. Zhang, B. Zhang, D. Chen, L. Yuan, and F. Wen, "Cross-domain correspondence learning for exemplar-based image translation," in *Proc. IEEE/CVF Conf. Comput. Vis. Pattern Recognit.*, 2020, pp. 5142–5152.

[50] U. Ojha et al., "Few-shot image generation via cross-domain correspondence," in *Proc. IEEE/CVF Conf. Comput. Vis. Pattern Recognit.*, 2021, pp. 10738–10747.

[51] Y. Zhao, H. Ding, H. Huang, and N.-M. Cheung, "A closer look at few-shot image generation," in *Proc. IEEE/CVF Conf. Comput. Vis. Pattern Recognit.*, 2022, pp. 9130–9140.

[52] J. R. Hershey and P. A. Olsen, "Approximating the Kullback Leibler divergence between Gaussian mixture models," in *Proc. IEEE Int. Conf. Acoust., Speech, Signal Process.*, 2007, vol. 4, pp. IV-317–IV-320.

[53] O. Ronneberger, P. Fischer, and T. Brox, "U-Net: Convolutional networks for biomedical image segmentation," in *Proc. Int. Conf. Med. Image Comput. Comput.-Assist. Interv.*, 2015, pp. 234–241.

[54] T.-H. Vu, H. Jain, M. Bucher, M. Cord, and P. Pérez, "Advent: Adversarial entropy minimization for domain adaptation in semantic segmentation," in *Proc. IEEE/CVF Conf. Comput. Vis. Pattern Recognit.*, 2019, pp. 2512–2521.

[55] Y. Yang and S. Soatto, "FDA: Fourier domain adaptation for semantic segmentation," in *Proc. IEEE/CVF Conf. Comput. Vis. Pattern Recognit.*, 2020, pp. 4084–4094.

[56] J. Hoffman et al., "CyCADA: Cycle-consistent adversarial domain adaptation," in *Proc. 35th Int. Conf. Mach. Learn.*, 2018, vol. 80, pp. 1989–1998. [Online]. Available: https://proceedings.mlr.press/v80/hoffman18a.html

[57] G. Vivone et al., "A critical comparison among pansharpening algorithms," *IEEE Trans. Geosci. Remote Sens.*, vol. 53, no. 5, pp. 2565–2586, May 2015.

[58] Y. Zou, Z. Yu, B. V. Kumar, and J. Wang, "Unsupervised domain adaptation for semantic segmentation via class-balanced self-training," in *Proc. Eur. Conf. Comput. Vis.*, 2018, pp. 297–313.

[59] K. Kamnitsas et al., "Unsupervised domain adaptation in brain lesion segmentation with adversarial networks," in *Proc. Int. Conf. Inf. Process. Med. Imag.*, 2017, pp. 597–609.

[60] M. E. Kalacska, L. S. Bell, G. Arturo Sanchez-Azofeifa, and T. Caelli, "The application of remote sensing for detecting mass graves: An experimental animal case study from Costa Rica," *J. Forensic Sci.*, vol. 54, no. 1, pp. 159–166, 2009, doi: 10.1111/j.1556-4029.2008.00938.x.

Kenichi Sasaki (Student Member, IEEE) received the B.S. and M.S. degrees in mechanical engineering from the Tokyo Institute of Technology, Tokyo, Japan, in 2016 and 2019, respectively. He is currently working toward the Ph.D. degree in aerospace engineering and sciences with the University of Colorado Boulder, Boulder, CO, USA.

He was involved in a small satellite development to work on a build-in camera for run-time semantic segmentation. His research focuses on satellite imagery analysis using deep learning techniques including semantic segmentation, change detection and domain adaptation. His current research topics are focused in ocean pollution monitoring using optical and SAR imagery.

Tatsuyuki Sekine (Member, IEEE) received the B.S. and M.S. degrees in high energy physics from the Tokyo Institute of Technology, Tokyo, Japan, in 2017 and 2019, respectively.

He was searching for new physics beyond the Standard Model by detecting signals from the huge particle collision data, collected from the LHC experiment in CERN. He currently joined Amanogi as an Engineer, who applies satellite imagery for measurements. His research interests include remote sensing for Earth observation, mainly using with satellite imagery. He is interested in space science, machine learning, and statistics.

William Emery (Fellow, IEEE) received the Ph.D. degree in physical oceanography from the University of Hawaii, Honolulu, HI, USA, in 1975.

He is currently an Adjunct Professor of informatics with Tor Vergata University, Rome, Italy. He was with Texas AM University, College Station, TX, USA. In 1978, he moved to The University of British Columbia, Vancouver, BC, Canada, where he created a Satellite Oceanography Facility/Education/Research Program. In 1987, he was appointed as a Professor of aerospace engineering sciences with the University of Colorado, Boulder, CO, USA. He has authored more than 182 refereed publications on both ocean and land remote sensing and three textbooks.

Dr. Emery is the Vice President for Publications of the IEEE Geoscience and Remote Sensing Society (GRSS) and a Member of the IEEE Periodicals Committee. He was a recipient of the IEEE GRSS Educational Award in 2004 and IEEE GRSS Outstanding Service Award in 2009 and the GRSS Fawaz Ulaby Distinguished Achievement Award for 2022. He is a Fellow of the American Meteorological Society (2010), the American Astronautical Society (2011), and the American Geophysical Union (2012). He was elected to the IEEE TAB Hall of Honor in 2021.